


Article

Facile Hydrothermal Synthesis of Nanocubic Pyrite Crystals Using Greigite Fe_3S_4 and Thiourea as Precursors

Xin Nie ¹, Suxing Luo ^{1,2,3}, Meizhi Yang ^{1,2}, Ping Zeng ^{1,2}, Zonghua Qin ¹, Wenbin Yu ¹ and Quan Wan ^{1,4,*} 

¹ State Key Laboratory of Ore Deposit Geochemistry, Institute of Geochemistry, Chinese Academy of Sciences, Guiyang 550081, China; niexin2004@163.com (X.N.); luosuxing123123@163.com (S.L.); yangmeizhi@mail.gyig.ac.cn (M.Y.); zengpeng@mail.gyig.ac.cn (P.Z.); qinzonghua@vip.gyig.ac.cn (Z.Q.); yuwenbin@mail.gyig.ac.cn (W.Y.)

² University of Chinese Academy of Sciences, Beijing 100049, China

³ Zunyi Normal College, Zunyi 563002, China

⁴ CAS Center for Excellence in Comparative Planetology, Hefei 230026, China

* Correspondence: wanquan@vip.gyig.ac.cn; Tel.: +86-0851-85891928

Received: 2 April 2019; Accepted: 29 April 2019; Published: 1 May 2019



Abstract: Nanocubic pyrite (FeS_2) crystals with exposed (100) crystal faces and sizes of 100–200 nm were successfully synthesized via a facile hydrothermal method using greigite (Fe_3S_4) as the iron precursor and thiourea (NH_2CSNH_2) as the sulfur source. When the concentration of thiourea was 40 mmol/L, both pyrite and hematite were observed in the as-prepared sample, indicating incomplete conversion of greigite into pyrite. With an increased thiourea concentration to 80 mmol/L, pyrite was found to be the only crystalline phase in the synthesized samples. All greigite could be transformed to pyrite within 24 h via the hydrothermal method, while further prolonging the hydrothermal time had insignificant effect on the crystal phase composition, crystallinity, and morphologies of the prepared nanocubic pyrite crystals. In contrast, when a mixture of Na_2S and S powder was used to replace the thiourea as the sulfur source, tetragonal, orthorhombic, cubic, and irregular pyrite crystal particles with sizes of 100 nm–1 μm were found to co-exist in the prepared samples. These results demonstrate the critical influence of sulfur source on pyrite morphology. Furthermore, our hydrothermal process, using a combination of greigite and thiourea, is proved to be effective in preparing nanocubic pyrite crystals. Our findings can also provide new insight into the formation environments and pathways of nanocubic pyrite under hydrothermal conditions.

Keywords: nanocubic pyrite; hydrothermal synthesis; greigite; thiourea

1. Introduction

Iron sulfides, particularly pyrite (FeS_2), are ubiquitous in various hydrothermal ore deposits as well as Earth surface environments, and their scientific merits have been demonstrated in many fundamental studies. For example, pyrite may provide essential information for better understanding the origin and evolution of early life on the Earth's surface environment and the global biogeochemical cycling of sulfur and iron [1,2]. Because pyrite is preferentially formed in anoxic conditions, and its morphology and chemical composition highly depends on the formation conditions, pyrite can also be used as a key geochemical indicator of contemporary environmental conditions in hydrothermal systems or Earth's surface system [1,3]. In addition, previous studies have documented that pyrite plays a crucial role in the transport, fate, reactivity, and the associated ecological toxicity of various

trace elements of economic or environmental importance, including the noble metal Au and toxic heavy metals [1,4–6].

On the application aspect, owing to its abundance, low cost, low toxicity, and high chemical reactivity, pyrite has been recognized as a promising material for effectively eliminating environmental contaminants in Earth's near-surface environment under anoxic and oxic conditions, including toxic heavy metals and metalloids, radionuclides, and organic pollutants (e.g., chlorinated organic pollutants, polycyclic aromatic hydrocarbons, organic dyes, and others) [7–15]. Moreover, thanks to its high optical absorption coefficient, unique electrical and semiconducting properties, and suitable band gap (0.95 eV), pyrite (especially micro-nanopyrite) has received extensive attention for its potential applications in electrocatalytic hydrogen evolution reactions (HERs), catalytic hydrogenation, high capacity lithium ion batteries, photovoltaics, photocatalysts, photoelectrochemical solar cells, and so on [16–19]. It should be noted the chemical composition (or purity), size, morphology, exposed surface facet, and microstructure can significantly affect the surface physicochemical properties of pyrite, and consequently impact its application performance [3]. Since naturally occurring pyrite inevitably contains significant quantities of impurities and crystal defects, undesirable variations in the physical and chemical properties are often presented in the application of natural pyrite. Therefore, synthesis of pure-phase pyrite with controllable morphology and specific facets is of great significance for their application and, thus, has attracted considerable research interest in recent years.

Over the past few decades, micro-nanopyrite crystals with various geometrical morphologies, microstructures (e.g., nanoparticles, nanowires, nanocubes, nano-octahedrons, and micro-spheres), and different sizes have been successfully synthesized using different synthetic methods, including hydrothermal methods [20–25], solvothermal synthesis [26–30], heating-up [31,32], the low-temperature aqueous method [33], sulphidation [34,35], chemical vapor deposition [36], hot-injection [31,37–39], electrochemical deposition [40], and sonosynthesis [41]. Among these fabrication methods, hydrothermal synthesis, usually conducted in an autoclave containing all precursors and a certain amount of water under high temperature and pressure, can provide excellent control over the size and morphology of pyrite and is relatively easy to implement [42]. Various Fe salts (including Fe(II) and Fe(III)), iron oxide (e.g., Fe_2O_3 , Fe_3O_4), FeS, FeS_m , $(\text{Fe}(\text{S}_2\text{CNEt}_2)_3)$, $[(\text{C}_2\text{H}_5\text{O})_2\text{P}(\text{S})\text{S}]_3\text{Fe}$, Na_2S or H_2S , $\text{Na}_2\text{S}_2\text{O}_3$, S, and thiourea can be used as precursors to fabricate micro-nanopyrite [42]. The type of precursor, hydrothermal temperature, pH, and surfactant may significantly affect the size and morphology of prepared pyrite. In a polysulfide pathway to synthesize pyrite, the initially formed amorphous FeS can be converted to a metastable intermediate greigite (Fe_3S_4), which is then transformed to pyrite via further sulfidation [19]. However, most previous studies focused on the transformation of greigite to pyrite at low temperatures (<100 °C); little research has been conducted at hydrothermal temperatures. Thus, there is direct experimental evidence to support the hypothesis that greigite transforms to pyrite under hydrothermal conditions [1,43]. Therefore, we thought that greigite should be a critical intermediate or precursor to synthesize micro-nanopyrite, and it may help to provide a direct evidence to reveal the formation mechanism of pyrite under hydrothermal conditions. Although a lot of hydrothermal progresses has been developed in controllable synthesis of micro-nanopyrite crystals, simultaneously use of greigite as the iron precursor and thiourea (NH_2CSNH_2) as the sulfur source has not been previously attempted, and the relevant reaction mechanisms also need to be further investigated.

In order to enhance our understanding of the formation mechanism of pyrite under hydrothermal conditions and provide new insight into synthesis of pyrite crystals, nanocubic pyrite crystals with exposed (100) crystal faces were successfully synthesized in this work via a facile hydrothermal method with greigite as the iron precursor and thiourea as the sulfur source. Crystal phase compositions and morphologies were characterized by X-ray diffraction (XRD) and field emission scanning electron microscopy (FESEM), respectively. The influences of reaction conditions, such as hydrothermal time, precursor concentration, as well as type of sulfur source on composition and morphology of nanocubic pyrite crystals, were also systematically investigated.

2. Materials and Methods

2.1. Chemicals and Materials

Sodium sulfide ($\text{Na}_2\text{S}\cdot 9\text{H}_2\text{O}$), ferrous sulfate ($\text{FeSO}_4\cdot 7\text{H}_2\text{O}$), thiourea (NH_2CSNH_2), sulfur (S) powder, hydrochloric acid (HCl) (36~38 wt%), and anhydrous ethanol ($\text{C}_2\text{H}_5\text{OH}$) were purchased from Sinopharm Chemical Reagent Co., Ltd. (Shanghai, China). All chemicals were of analytical or guaranteed reagent grade and were used without further purification. Deionized water with a resistivity of $18.2\text{ M}\Omega\cdot\text{cm}$ was obtained from a Millipore synergy UV system (Millipore Corporation, Molsheim, Alsace, France), and deoxygenated deionized water was used in all experiments.

2.2. Synthesis of the Greigite Precursor

Greigite precursor was prepared by a refluxing method. In a typical process, 100 mL of 0.1 mol/L $\text{FeSO}_4\cdot 7\text{H}_2\text{O}$ solution was added to 100 mL of 0.1 mol/L $\text{Na}_2\text{S}\cdot 9\text{H}_2\text{O}$ boiling solution in a three-neck flask under vigorous stirring and degassing with Ar. A black precipitate appeared immediately. Subsequently, the solution was refluxed at $100\text{ }^\circ\text{C}$ for 3 h and then naturally cooled to room temperature. The resulting black precipitation was centrifuged for 5 min (4000 rpm) and then washed with deoxygenated deionized water three times and anhydrous ethanol three times. Finally, the product was dried at $40\text{ }^\circ\text{C}$ for 24 h in a vacuum oven (DZF-6050, Shanghai Shenxian Thermostatic Equipment, Shanghai, China).

2.3. Synthesis of Pyrite Nanocubic Crystals

Pyrite samples were prepared using a hydrothermal approach. In a typical process, 0.88 g Fe_3S_4 precursor was added to 60 mL of thiourea solution with different concentrations under vigorous stirring at room temperature. The mixture was then transferred to a 100 mL Teflon-line autoclave, and then hydrothermally treated at $200\text{ }^\circ\text{C}$ in an oven for different times. After the hydrothermal reaction, the resulting black product was collected by centrifugation. Then it was thoroughly washed with 30 mL of 1 mol/L HCl, 1 mol/L of Na_2S boiling solution, and deoxygenated deionized water three times, respectively, and anhydrous ethanol ten times. Finally, the obtained black product was dried at $40\text{ }^\circ\text{C}$ for 6 h in a vacuum oven and then stored in a glove box with an anaerobic environment. The crystal phase composition and crystallinity were determined by X-ray diffraction (XRD, Empyrean, PANalytical B.V, Almelo, The Netherlands) operating with $\text{Cu-K}\alpha$ radiation. The surface morphologies of the resulting samples were characterized using scanning electron microscopy (SEM, Scios, FEI Company, Hillsboro, OR, USA) with an acceleration voltage of 30.0 kV. To investigate the effect of sulfur source on the structure and morphology of pyrite, thiourea was replaced by a boiling mixture of Na_2S and S powder.

3. Results and Discussion

3.1. Characterization of the Greigite Fe_3S_4 Precursor

The crystal phase composition and crystallinity of the as-prepared greigite product were characterized by X-ray diffraction (XRD), and the corresponding XRD pattern is shown in Figure 1. All diffraction peaks were consistent with cubic greigite (Fe_3S_4 , JCPDS no. 16-0713) with $Fd\bar{3}m$ space group. The dominant characteristic diffraction peaks of the XRD pattern at $2\theta = 15.48^\circ$, 25.43° , 29.96° , 36.34° , 47.81° , and 52.36° were attributed to the (111), (220), (311), (400), (511), and (440) planes of greigite (Fe_3S_4), respectively. Greigite was found to be the only crystalline phase in the sample, and the intermediate (e.g., FeS) was undetectable by XRD. The characteristic diffraction peaks appeared weak and broad, implying low purity and crystallinity of greigite precursor. Similar with its oxide analogue magnetite Fe_3O_4 , greigite is an inverse spinel with a general formula AB_2X_4 , where A is nominally a, Fe^{2+} , B is a, Fe^{3+} and X is a S^{2-} . Greigite shows typical ferromagnetic behavior because of the presence of unpaired electrons (data not shown here) [1]. The unit cell of greigite is face-centered

cubic. It consists of 32 close packed atoms of sulfur and 24 atoms of iron with a $\text{Fe}^{2+}/\text{Fe}^{3+}$ ratio of 1:2, where Fe^{2+} atoms occur in tetrahedral sites, and mixed Fe^{2+} and Fe^{3+} occur in the octahedral sites coordinated with S^{2-} [44]. Greigite could be formed directly through the rapid autoxidation reaction of pre-existing mackinawite (FeS_m , formed after mixing Fe(II) and S(-II) solutions) in anoxic H_2O at temperatures somewhat above $70\text{ }^\circ\text{C}$ [1].

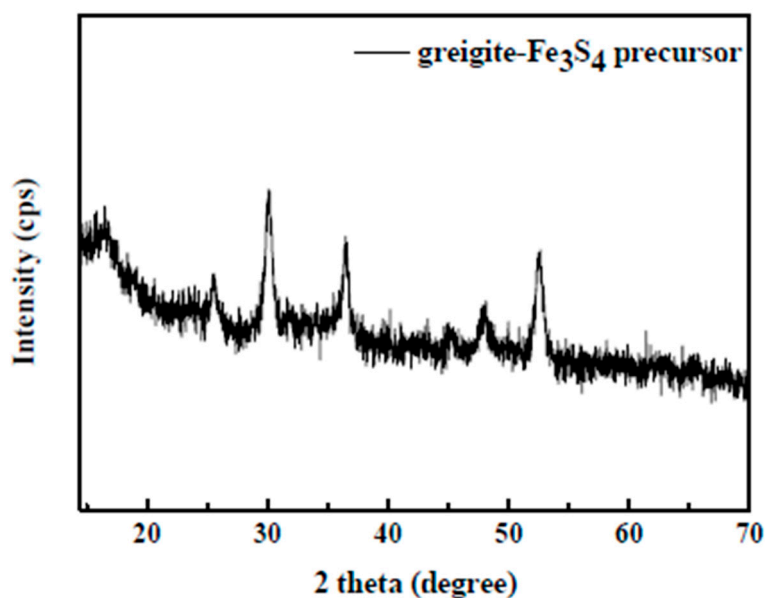


Figure 1. X-ray diffraction (XRD) pattern of the obtained greigite precursor.

3.2. Characterization of Pyrite Nanocubes Prepared with Thiourea as the Sulfur Source

3.2.1. Effect of Hydrothermal Time

Figure 2a shows the XRD patterns for the samples prepared at different hydrothermal times in 80 mmol/L thiourea solution. It can be seen that the XRD patterns of all samples exhibited similar characteristics. The diffraction peaks at $2\theta = 28.51^\circ, 33.08^\circ, 37.11^\circ, 40.78^\circ, 47.41^\circ, 56.28^\circ, 59.02^\circ, 61.69^\circ, 64.28^\circ, 76.60^\circ,$ and 78.96° were well attributed to the (111), (200), (210), (211), (220), (311), (222), (023), (321), (331), and (420) planes of cubic pyrite (FeS_2) (JCPDS card no. 42-1340) with a space group of $Pa\bar{3}$, respectively [45–48]. Pyrite was found to be the only crystalline phase in all prepared samples at different hydrothermal times. No other impure phases (e.g., greigite (Fe_3S_4), pyrrhotite ($\text{Fe}_{(1-x)}\text{S}$), marcasite (FeS_2), or other impurities) appeared, implying high phase-purity of pyrite in these samples. The characteristic diffraction peaks were sharp and narrow, confirming good crystallization of these samples. Additionally, the diffraction peak intensities and the peak widths of pyrite were found to be almost identical, with increases of hydrothermal times from 24 to 168 h, indicating that all the greigite could be thoroughly transformed to pyrite within 24 h via hydrothermal method with thiourea as the precursor. Further prolonging the hydrothermal time had no significant effect on the crystal phase composition and crystallization of the product.

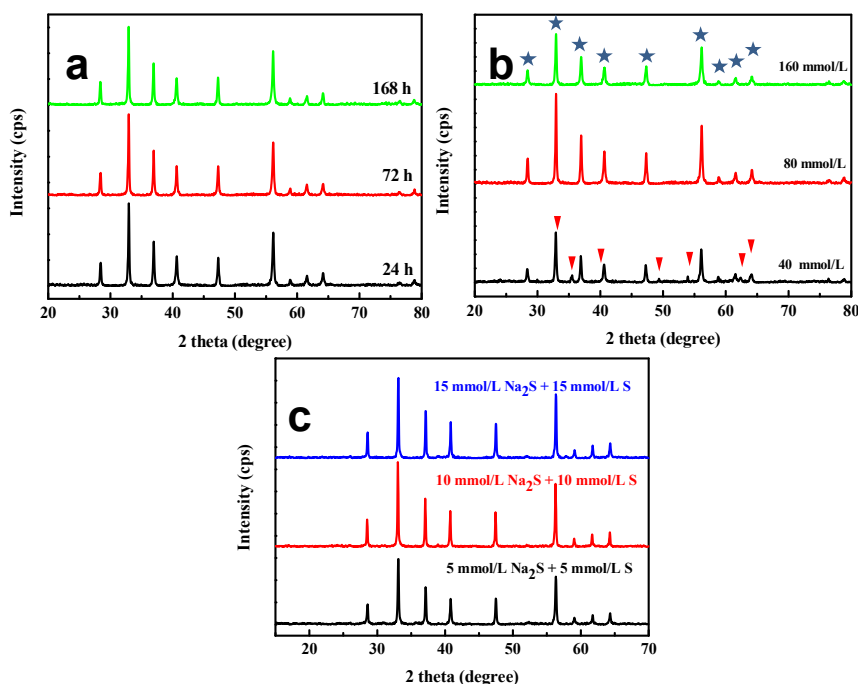


Figure 2. (a) XRD patterns of pyrite samples prepared at different hydrothermal times in 80 mmol/L thiourea solution; (b) XRD patterns of samples prepared at 24 h with different concentrations of thiourea, ★: pyrite, ▼: hematite; and (c) XRD patterns of the as-synthesized pyrite at 24 h with different concentrations of Na₂S and S powder as the sulfur source.

To investigate the effect of hydrothermal time on the morphologies and microstructures of the samples, the as-synthesized samples were characterized by SEM. As shown in Figure 3, pyrite in all samples obtained with a hydrothermal time from 24 to 168 h exhibited individual nanocubic shapes with smooth surfaces, implying that screw-dislocation or two-dimensional nucleation growth might be the dominant growth mechanisms of pyrite crystal [43]. The edge length of the nanocubes was approximately 100–200 nm. With hydrothermal time increased from 24 to 168 h, the morphologies and microstructures of nanocubic pyrite in all samples showed no noticeable changes. The average edge length of the nanocubes was statistically analyzed to be about 115, 112, and 120 nm for the samples prepared at 24, 72, and 168 h, respectively, indicating that the crystal growth process could be completed within 24 h. The EDX result (Figure 4) further confirmed that the pyrite was composed of Fe and S elements, with a molar ratio of S/Fe of approximately two, supporting that the prepared product was pure pyrite (FeS₂). Moreover, the dominant facet on nanocubic crystals pyrite was the (100) facet, indicating that the cubic structure was the most stable structure than others under our experimental conditions. In fact, the major surface crystallographic planes of pyrite included (100), (111), (210), and (110), and their surface energies were 1.06, 1.40, 1.50, and 1.68 J/m², respectively, suggesting that the surface energy of the (100) was the lowest. Thus, the (100) crystal face was considered to be the most stable [2,42]. Accordingly, crystal growth along the (110), (210), and (111) directions was expected to be more favorable than the (100) direction, leading to the formation of a cubic structure with exposed (100) crystal face, which was consistent with observations of the most common naturally occurring and synthetic pyrites [49].

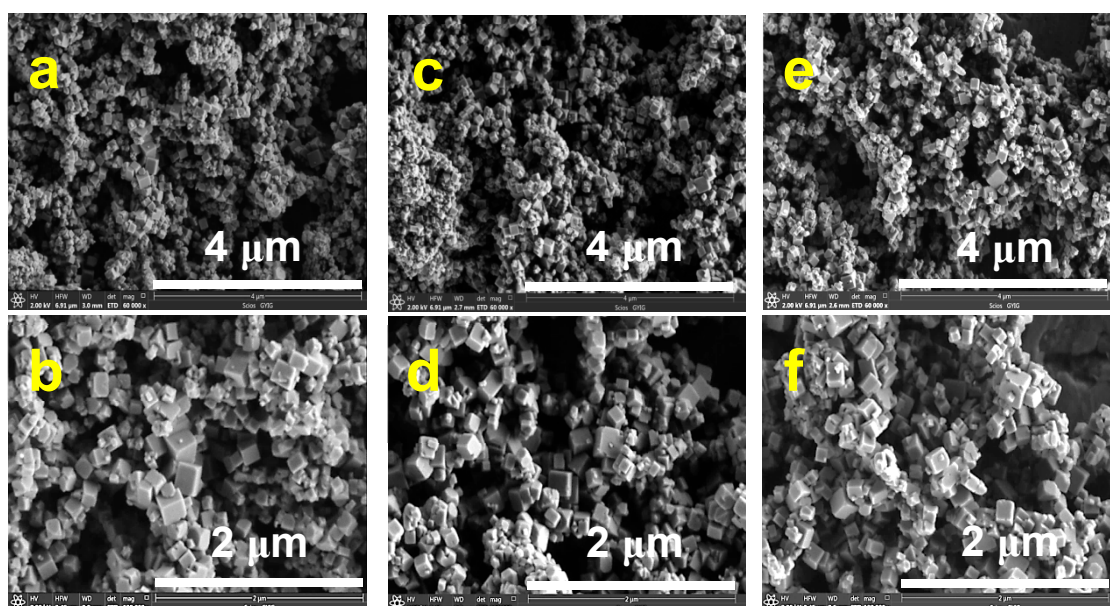


Figure 3. Scanning electron microscopy (SEM) images of the as-synthesized pyrite nanocrystals with 80 mmol/L thiourea as the sulfur source at 24 (a,b), 72 (c,d), and 168 h (e,f), respectively.

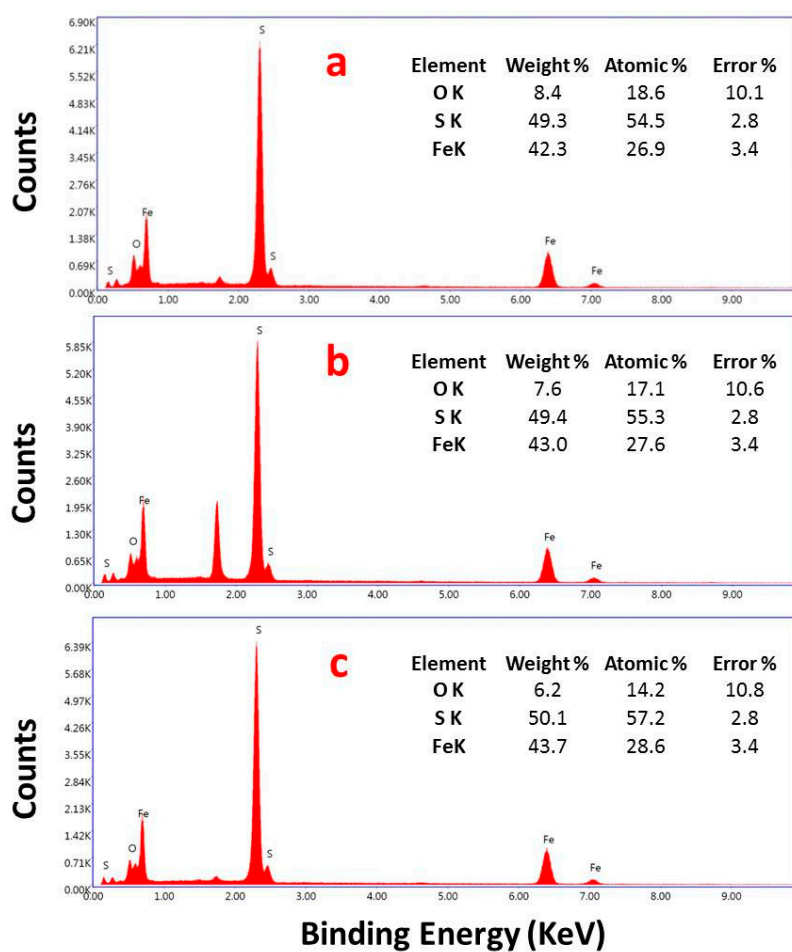


Figure 4. Energy-dispersive X-ray spectrum (EDS) of the as-synthesized pyrite nanocrystals with 80 mmol/L thiourea as the sulfur source at 24 (a), 72 (b), and 168 h (c), respectively.

3.2.2. Effect of the Thiourea Concentration

To further investigate the effect of thiourea on the pyrite prepared from greigite, hydrothermal experiments were conducted with different concentrations of thiourea at 24 h. Figure 2b shows the XRD patterns of the samples prepared with different thiourea concentrations. It was clearly seen that the phase compositional characteristics of the prepared product seemed to depend essentially on the thiourea concentration. When the thiourea concentration was 40 mmol/L, besides the clearly observed characteristic diffraction peaks of pyrite, several other diffraction peaks could be seen, which were attributed to a small amount of hematite (Fe_2O_3) formed under this condition. Specifically, the diffraction peaks agreed well with hexagonal scalenohedral hematite (JCPDS no. 33-0664). The peaks at $2\theta = 33.15^\circ$, 35.61° , 40.85° , 49.48° , 54.09° , 62.45° , and 63.99° can be indexed to the (104), (110), (113), (024), (116), (214), and (300) planes of hematite, respectively. This phenomenon suggests that a low concentration of thiourea was not sufficient to completely convert the greigite into pyrite. Increasing the concentration of thiourea resulted in an increase of pyrite content, simultaneously accompanied by a decrease in the amount of hematite in the as-synthesized samples. When the concentration of thiourea increased to 80 mmol/L, the XRD diffraction peaks of hematite vanished completely, and pyrite was found to be the only crystalline phase in the samples, suggesting that all greigite could be transformed into pyrite with the addition of 80 mmol/L thiourea. The XRD peak intensities of pyrite became remarkably stronger, and the peak widths became narrower, indicating an increase in the crystal size and crystallinity of pyrite. However, with a further increase in thiourea concentration to 160 mmol/L, the XRD peak intensities of pyrite decreased significantly, suggesting that high concentration of thiourea might inhibit the growth of pyrite crystals.

Figure 5 shows the effect of the thiourea concentration on the morphologies of the as-prepared product at 24 h. The morphologies and sizes of the obtained samples were also strongly dependent on the thiourea concentration used in the reaction. When the concentration of thiourea was 40 mmol/L (Figure 5a,b), the SEM images revealed that the resulting product consisted of nanocubic pyrite particles (with an average particle size of ~100 nm) with exposed (100) crystal faces and a fraction of hematite nanocrystals with polyhedral bipyramid (marked with yellow dotted circle) with the particle size of 100–200 nm. This indicated that a low concentration of thiourea resulted in conversion of a fraction of greigite into hematite Fe_2O_3 because of the shortage of the sulfur source. The EDX result (Figure 6a) also validated that a significantly higher content of O existed in this sample, owing to the presence of hematite Fe_2O_3 . When the concentration of thiourea was increased to 80 mmol/L (Figure 5c,d), it was clearly seen that only nanocubic pyrite could be observed in the SEM images, and the content of O in the sample remarkably decreased (Figure 6b). The average particle size of nanocubic pyrite was found to increase significantly to ~115 nm, indicating an increase of thiourea content was conducive to the growth of nanocubic pyrite crystal, which was consistent with the XRD results. However, with the further increase of the thiourea concentration to 160 mmol/L (Figure 5e,f), no obvious morphological changes could be observed, except for a slight decrease of the particle size of nanocubic pyrite (with the average particle size of ~110 nm), and the individual nanocubic pyrite appeared more uniform. This may be attributed an overly high concentration of thiourea in the solution that could inhibit the growth of pyrite crystals, implying that the morphologies and microstructures of the as-synthesized product could be controlled by the concentration of thiourea used as the sulfur source.

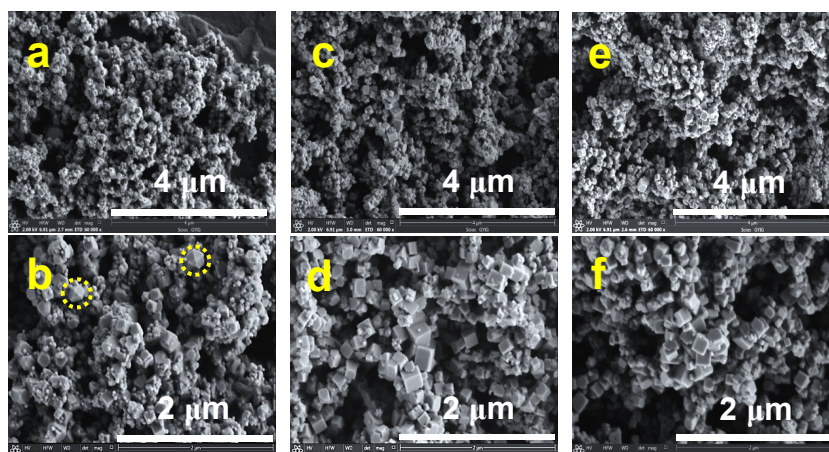


Figure 5. SEM images of the as-synthesized pyrite nanocrystals at 24 h with different concentrations of thiourea as the sulfur source: (a,b) 40 mmol/L, (c,d) 80 mmol/L, and (e,f) 160 mmol/L.

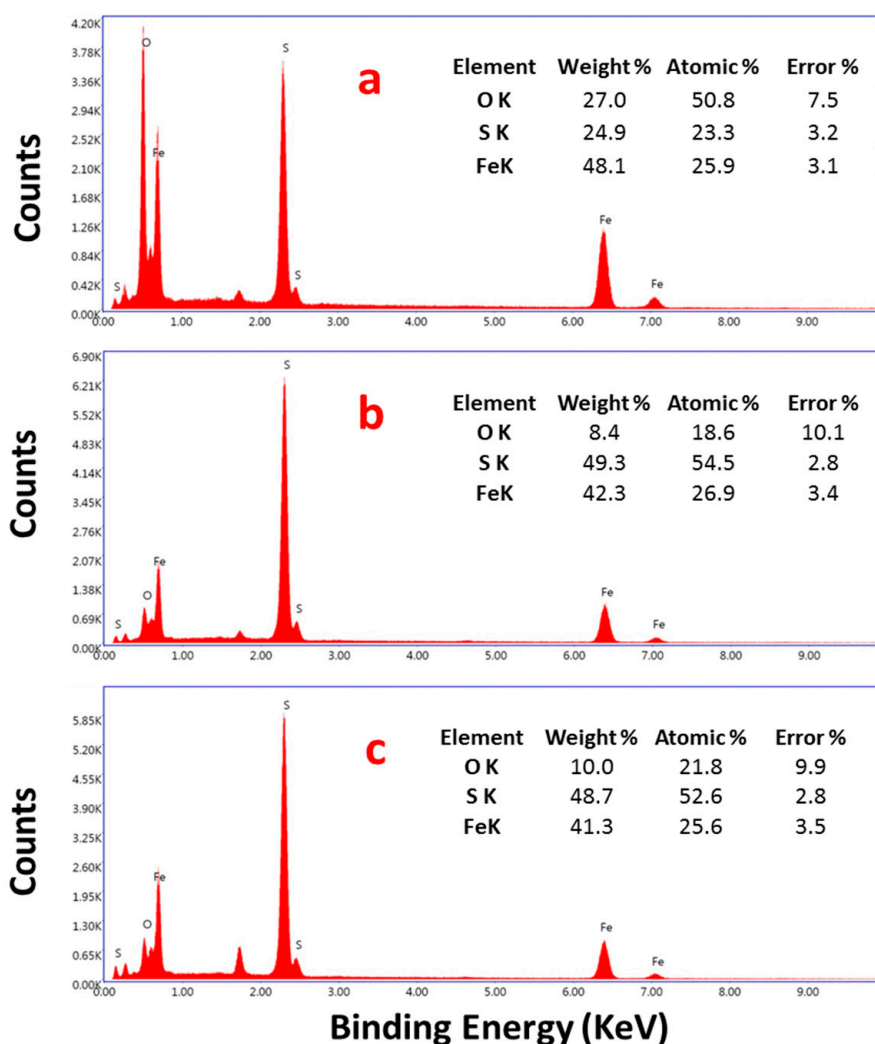


Figure 6. Energy-dispersive X-ray spectrum of the as-synthesized pyrite nanocrystals at 24 h with different concentrations of thiourea as the sulfur source: (a) 40 mmol/L, (b) 80 mmol/L, and (c) 160 mmol/L.

3.3. Characterization of Pyrite Prepared with a Mixture of Na₂S and S Powder as the Sulfur Source

To further investigate the influence of the type of sulfur source on the synthesis of pyrite, a mixture of Na₂S and S powder was used as the sulfur source to react with greigite precursor. Figure 2c displays the XRD patterns of the as-synthesized pyrite at 24 h with different concentrations of Na₂S and S powder as the sulfur source. As shown, the diffraction peaks of all obtained samples were very similar and could be well-indexed as pyrite. No other characteristic diffraction peaks could be found, indicating that the mixture of 5 mmol/L Na₂S and 5 mmol/L S powder was enough to transform greigite into pure pyrite, and the concentrations of Na₂S and S powder has no remarkable influence on the crystal phase of these products. Furthermore, with increasing concentration of Na₂S and S powder, the diffraction peak intensities of pyrite significantly increased in pace with the narrowing of the peak width, meaning an increase in the crystallinity of pyrite, which implied that a high concentration of mixture of Na₂S and S powder may be conducive to the growth of pyrite crystal particles.

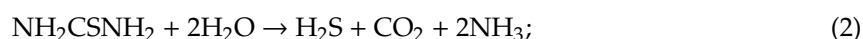
The effect of the concentration of Na₂S and S powder on the morphologies and microstructures of the resulting pyrite with Na₂S and S powder as sulfur source was also investigated by SEM (shown in Figure 7). Compared with pyrite nanocrystals synthesized with thiourea as the sulfur source, the SEM images revealed that the as-synthesized iron pyrite crystals with Na₂S and S powder as the sulfur source had completely different morphologies, in which tetragonal, orthorhombic, cubic, and irregular pyrite crystal particles with sizes of 0.1–1 μm could be observed in all prepared samples. The co-existence of various morphologies and microstructures of pyrite indicated that the sulfur source had a significant influence on pyrite morphologies. When the concentrations of both Na₂S and S powder were increased from 5 to 15 mmol/L, no obvious morphological changes in pyrite were observed. The discrepancy of morphologies may be attributed to the different nucleation-growth process originating from the sulfur source.

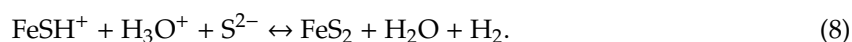
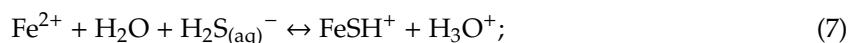
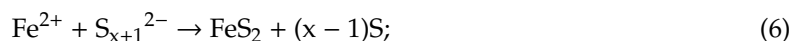
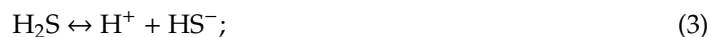


Figure 7. SEM images of the as-synthesized pyrite crystals at 24 h with Na₂S and S powder as the sulfur source: (a) 5 mmol/L Na₂S + 5 mmol/L S powder, (b) 10 mmol/L Na₂S + 10 mmol/L S powder, and (c) 15 mmol/L Na₂S + 15 mmol/L S powder.

3.4. Mechanism of Pyrite Formation

Based on the above results, it can be speculated that pyritization of greigite is a dissolution-precipitation process. The dissolution of greigite in water can produce ferrous (Fe²⁺), S²⁻, and zero-valence sulfur S [1]. Thiourea (NH₂CSNH₂) can react with H₂O to form small molecules of H₂S, CO₂, and NH₃ at high temperature. Dissolved H₂S in aqueous solution can be deprotonated to obtain HS⁻ and S²⁻. S²⁻ can react with S to form aqueous polysulfide species S_{x+1}²⁻ at high temperature. A high concentration of S²⁻ is beneficial to the formation of pyrite. The Fe²⁺ species originating from dissolved greigite can further react with S_{x+1}²⁻ or H₂S to produce FeS₂ nuclei when the solution is supersaturated (with respect to pyrite). The consumption of Fe²⁺ in the solution would further facilitate the dissolution of greigite in water, leading to the growth of FeS₂ nuclei to form pyrite crystals. The reaction process and relative mechanism between greigite and thiourea as well as the mixture of Na₂S and S powder can be described as below [49]:





The growth of nanocubic pyrite via a hydrothermal method with greigite as the iron precursor and thiourea as the sulfur source has not been reported to date. Furthermore, as deduced from our results, it can be concluded that the sulfur precursor plays a crucial role in controlling the crystal phase composition, morphology, and size of the as-prepared pyrite with greigite as the iron precursor. Using thiourea as the sulfur source, the obtained product had a narrower size distribution as well as smaller crystal sizes compared with that of mixture of Na_2S and S powder as the sulfur source. Additionally, the morphology and particle size of pyrite crystals greatly depended on the rates of dissolution of greigite, the formation pathway of pyrite, and the initial supersaturation with respect to pyrite. When the mixture of Na_2S and S powder was used as the sulfur source, pyrite was formed through the reaction between Fe^{2+} and polysulfide via Equation (6) [1]. If thiourea was used as the sulfur source, the formation of pyrite was achieved mainly through Equations (7) and (8) [49]. When initial supersaturation (with respect to pyrite) is low, large-sized pyrite crystals will form, owing to that only a few pyrite nuclei can be formed. In contrast, fine-grained pyrite crystals would be the dominant product at high initial supersaturation (with respect to pyrite) because of a significant increase in the number of pyrite nuclei [43]. Therefore, in our experimental system, a much smaller particle size and a narrower size distribution of pyrite crystals were obtained with thiourea as the sulfur source, compared with that of the mixture of Na_2S and S powder as the sulfur source, because of the significantly higher concentration of the sulfur source for thiourea, which enhanced supersaturation (with respect to pyrite) and consequently facilitated the formation of numerous nuclei of pyrite crystals [49].

4. Conclusions

In summary, nanocubic pyrite crystals with exposed (100) crystal faces and edge lengths of approximately 100–200 nm were fabricated via a facile hydrothermal method with greigite as the iron precursor and thiourea as the sulfur source. The Fe_3S_4 precursor was prepared by a refluxing method via mixing $\text{FeSO}_4 \cdot 7\text{H}_2\text{O}$ and $\text{Na}_2\text{S} \cdot 9\text{H}_2\text{O}$ at 100 °C for 3 h. All the greigite could be thoroughly transformed to pyrite within 24 h via the hydrothermal method with thiourea as a precursor, and further prolonging the hydrothermal times had no significant effect on the crystal phase composition and crystallization of product. By varying the hydrothermal time from 24 to 168 h, the morphologies and microstructures of nanocubic pyrite showed no noticeable changes. When the concentration of thiourea was 40 mmol/L, pyrite as well as hematite could be observed, which was ascribed to the low concentration of thiourea insufficient to completely convert the greigite into pyrite. Moreover, when the mixture of Na_2S and S powder was used as the sulfur source, tetragonal, orthorhombic, cubic, and irregular pyrite crystal particles with sizes of 100 nm–1 μm could be observed in prepared samples, indicating that the sulfur source had significant influence on the morphologies and microstructures of pyrite. The results obtained in this study may provide new insights for synthesizing nanocubic pyrite crystal with controllable morphology and help to better understand the formation mechanism of pyrite. Our findings can also provide new insights into the formation environments and pathways of nanocubic pyrite under hydrothermal conditions.

Author Contributions: Q.W. proposed the research direction and guided the project; X.N. performed the experiment and wrote this manuscript; S.L., M.Y., and P.Z. analyzed the data and discussed the results; Z.Q. and W.Y. provided some useful suggestions.

Funding: This work was financially supported by the Chinese Academy of Sciences (“Hundred Talents Program”), the National Natural Science Foundation of China (41173074, 41872046), Guizhou Provincial Science and Technology projects ([2018]1172, [2019]1460), the Opening Fund of State Key Laboratory of Ore Deposit Geochemistry (201602), and the Training Project of Zunyi Municipal Innovative Talents Team (201539).

Acknowledgments: In this section you can acknowledge any support given which is not covered by the author contribution or funding sections. This may include administrative and technical support, or donations in kind (e.g., materials used for experiments).

Conflicts of Interest: The authors declare no conflict of interest.

References

1. Rickard, D.; Luther, G.W. Chemistry of iron sulfides. *Chem. Rev.* **2007**, *107*, 514–562. [[CrossRef](#)]
2. Vaughan, D.J.; Corkhill, C.L. Mineralogy of Sulfides. *Elements* **2017**, *13*, 81–87. [[CrossRef](#)]
3. Huang, F.; Gao, W.; Gao, S.; Meng, L.; Zhang, Z.; Yan, Y.; Ren, Y.; Li, Y.; Liu, K.; Xing, M.; et al. Morphology Evolution of Nano-Micron Pyrite: A Review. *J. Nanosci. Nanotechnol.* **2017**, *17*, 5980–5995. [[CrossRef](#)]
4. Large, R.R.; Danyushevsky, L.; Hollit, C.; Maslennikov, V.; Meffre, S.; Gilbert, S.; Bull, S.; Scott, R.; Emsbo, P.; Thomas, H.; et al. Foster, Gold and Trace Element Zonation in Pyrite Using a Laser Imaging Technique: Implications for the Timing of Gold in Orogenic and Carlin-Style Sediment-Hosted Deposits. *Econ. Geol.* **2009**, *104*, 635–668. [[CrossRef](#)]
5. Reich, M.; Kesler, S.E.; Utsunomiya, S.; Palenik, C.S.; Chryssoulis, S.L.; Ewing, R.C. Solubility of gold in arsenian pyrite. *Geochim. Cosmochim. Acta* **2005**, *69*, 2781–2796. [[CrossRef](#)]
6. Deditius, A.P.; Reich, M.; Kesler, S.E.; Utsunomiya, S.; Chryssoulis, S.L.; Walshe, J.; Ewing, R.C. The coupled geochemistry of Au and As in pyrite from hydrothermal ore deposits. *Geochim. Cosmochim. Acta* **2014**, *140*, 644–670. [[CrossRef](#)]
7. Liu, W.; Wang, Y.; Ai, Z.; Zhang, L. Hydrothermal Synthesis of FeS₂ as a High-Efficiency Fenton Reagent to Degrade Alachlor via Superoxide-Mediated Fe(II)/Fe(III) Cycle. *ACS Appl. Mater. Interface* **2015**, *7*, 28534–28544. [[CrossRef](#)] [[PubMed](#)]
8. Zhang, P.; Yuan, S.H. Production of hydroxyl radicals from abiotic oxidation of pyrite by oxygen under circumneutral conditions in the presence of low-molecular-weight organic acids. *Geochim. Cosmochim. Acta* **2017**, *218*, 153–166. [[CrossRef](#)]
9. Lee, W.; Batchelor, B. Abiotic, reductive dechlorination of chlorinated ethylenes by iron-bearing soil minerals. 2. Green rust. *Environ. Sci. Technol.* **2002**, *36*, 5348–5354. [[CrossRef](#)] [[PubMed](#)]
10. Lee, W.; Batchelor, B. Abiotic reductive dechlorination of chlorinated ethylenes by iron-bearing soil minerals. 1. Pyrite and magnetite. *Environ. Sci. Technol.* **2002**, *36*, 5147–5154. [[CrossRef](#)]
11. Pham, H.T.; Kitsuneduka, M.; Hara, J.; Suto, K.; Inoue, C. Trichloroethylene transformation by natural mineral pyrite: The deciding role of oxygen. *Environ. Sci. Technol.* **2008**, *42*, 7470–7475. [[CrossRef](#)]
12. Shukla, S.; Xing, G.; Ge, H.; Prabhakar, R.R.; Mathew, S.; Su, Z.; Nalla, V.; Venkatesan, T.; Mathews, N.; Sritharan, T.; et al. Origin of Photocatalytic Losses in Iron Pyrite (FeS₂) Nanocubes. *ACS Nano* **2016**, *10*, 4431–4440. [[CrossRef](#)] [[PubMed](#)]
13. Khalid, S.; Ahmed, E.; Khan, Y.; Riaz, K.N.; Malik, M.A. Nanocrystalline Pyrite for Photovoltaic Applications. *Chemistryselect* **2018**, *3*, 6488–6524. [[CrossRef](#)]
14. Cui, M.M.; Johannesson, K.H. Comparison of tungstate and tetrathiotungstate adsorption onto pyrite. *Chem. Geol.* **2017**, *464*, 57–68. [[CrossRef](#)]
15. Kantar, C.; Ari, C.; Keskin, S. Comparison of different chelating agents to enhance reductive Cr(VI) removal by pyrite treatment procedure. *Water Res.* **2015**, *76*, 66–75. [[CrossRef](#)]
16. Kirkeminde, A.; Ren, S. Thermodynamic control of iron pyrite nanocrystal synthesis with high photoactivity and stability. *J. Mater. Chem. A* **2013**, *1*, 49–54. [[CrossRef](#)]
17. Kuo, T.R.; Chen, W.T.; Liao, H.J.; Yang, Y.H.; Yen, H.C.; Liao, T.W.; Wen, C.Y.; Lee, Y.C.; Chen, C.C.; Wang, D.Y. Improving Hydrogen Evolution Activity of Earth-Abundant Cobalt-Doped Iron Pyrite Catalysts by Surface Modification with Phosphide. *Small* **2017**, *13*, 1603356. [[CrossRef](#)]
18. Zhu, Y.; Fan, X.; Suo, L.; Luo, C.; Gao, T.; Wang, C. Electrospun FeS₂@Carbon Fiber Electrode as a High Energy Density Cathode for Rechargeable Lithium Batteries. *ACS Nano* **2016**, *10*, 1529–1538. [[CrossRef](#)]
19. Igarashi, K.; Yamamura, Y.; Kuwabara, T. Natural synthesis of bioactive greigite by solid-gas reactions. *Geochim. Cosmochim. Acta* **2016**, *191*, 47–57. [[CrossRef](#)]

20. Yang, Z.; Liu, X.; Feng, X.; Cui, Y.; Yang, X. Hydrothermal synthesized micro/nano-sized pyrite used as cathode material to improve the electrochemical performance of thermal battery. *J. Appl. Electrochem.* **2014**, *44*, 1075–1080. [[CrossRef](#)]
21. Wang, D.; Wang, Q.; Wang, T. Shape controlled growth of pyrite FeS₂ crystallites via a polymer-assisted hydrothermal route. *Crystengcomm* **2010**, *12*, 3797–3805. [[CrossRef](#)]
22. Golsheikh, A.M.; Huang, N.M.; Lim, H.N.; Chia, C.H.; Harrison, I.; Muhamad, M.R. One-pot hydrothermal synthesis and characterization of FeS₂ (pyrite)/graphene nanocomposite. *Chem. Eng. J.* **2013**, *218*, 276–284. [[CrossRef](#)]
23. Wu, R.; Zheng, Y.F.; Zhang, X.G.; Sun, Y.F.; Xu, J.B.; Jian, J.K. Hydrothermal synthesis and crystal structure of pyrite. *J. Cryst. Growth* **2004**, *266*, 523–527. [[CrossRef](#)]
24. Zou, J.; Gao, J. Preparation of Nanosize Iron Pyrite FeS₂ and Its Properties. In *Materials Research, Pts 1 and 2*; Gu, Z.W., Han, Y.F., Pan, F.H., Wang, X.T., Weng, D., Zhou, S.X., Eds.; Trans Tech Publications Ltd.: Zurich, Switzerland, 2009; pp. 459–462.
25. Luo, S.; Nie, X.; Yang, M.; Fu, Y.; Zeng, P.; Wan, Q. Sorption of Differently Charged Gold Nanoparticles on Synthetic Pyrite. *Minerals* **2018**, *8*, 428. [[CrossRef](#)]
26. Liu, W.L.; Rui, X.H.; Tan, H.T.; Xu, C.; Yan, Q.Y.; Hng, H.H. Solvothermal synthesis of pyrite FeS₂ nanocubes and their superior high rate lithium storage properties. *RSC Adv.* **2014**, *4*, 48770–48776. [[CrossRef](#)]
27. Kar, S.; Chaudhuri, S. Solvothermal synthesis of nanocrystalline FeS₂ with different morphologies. *Chem. Phys. Lett.* **2004**, *398*, 22–26. [[CrossRef](#)]
28. Zhu, L.; Richardson, B.J.; Yu, Q. Controlled colloidal synthesis of iron pyrite FeS₂ nanorods and quasi-cubic nanocrystal agglomerates. *Nanoscale* **2014**, *6*, 1029–1037. [[CrossRef](#)] [[PubMed](#)]
29. Jiang, F.; Peckler, L.T.; Muscat, A.J. Phase Pure Pyrite FeS₂ Nanocubes Synthesized Using Oleylamine as Ligand, Solvent, and Reductant. *Cryst. Growth Des.* **2015**, *15*, 3565–3572. [[CrossRef](#)]
30. Yu, B.B.; Zhang, X.; Jiang, Y.; Liu, J.; Gu, L.; Hu, J.S.; Wan, L.J. Solvent-Induced Oriented Attachment Growth of Air-Stable PhasePure Pyrite FeS₂ Nanocrystals. *J. Am. Chem. Soc.* **2015**, *137*, 2211–2214. [[CrossRef](#)]
31. Macpherson, H.A.; Stoldt, C.R. Iron Pyrite Nanocubes: Size and Shape Considerations for Photovoltaic Application. *ACS Nano* **2012**, *6*, 8940–8949. [[CrossRef](#)]
32. Bai, Y.X.; Yeom, J.; Yang, M.; Cha, S.H.; Sun, K.; Kotov, N.A. Universal Synthesis of Single-Phase Pyrite FeS₂ Nanoparticles, Nanowires, and Nanosheets. *J. Phys. Chem. C* **2013**, *117*, 2567–2573. [[CrossRef](#)]
33. Morin, G.; Noël, V.; Menguy, N.; Brest, J.; Baptiste, B.; Tharaud, M.; Ona-Nguema, G.; Ikogou, M.; Viollier, E.; Juillot, F. Nickel accelerates pyrite nucleation at ambient temperature. *Geochem. Perspect. Lett.* **2017**, *5*, 6–11. [[CrossRef](#)]
34. Caban-Acevedo, M.; Liang, D.; Chew, K.S.; DeGrave, J.P.; Kaiser, N.S.; Jin, S. Synthesis, Characterization, and Variable Range Hopping Transport of Pyrite (FeS₂) Nanorods, Nanobelts, and Nanoplates. *ACS Nano* **2013**, *7*, 1731–1739. [[CrossRef](#)] [[PubMed](#)]
35. Wang, M.D.; Xing, C.C.; Cao, K.; Zhang, L.; Liu, J.B.; Meng, L. Template-directed synthesis of pyrite (FeS₂) nanorod arrays with an enhanced photoresponse. *J. Mater. Chem. A* **2014**, *2*, 9496–9505. [[CrossRef](#)]
36. Berry, N.; Cheng, M.; Perkins, C.L.; Limpinsel, M.; Hemminger, J.C.; Law, M. Atmospheric-Pressure Chemical Vapor Deposition of Iron Pyrite Thin Films. *Adv. Energy Mater.* **2012**, *2*, 1124–1135. [[CrossRef](#)]
37. Hsiao, S.-C.; Hsu, C.-M.; Chen, S.-Y.; Perng, Y.-H.; Chueh, Y.-L.; Chen, L.-J.; Chou, L.-H. Facile synthesis and characterization of high temperature phase FeS₂ pyrite nanocrystals. *Mater. Lett.* **2012**, *75*, 152–154. [[CrossRef](#)]
38. Yuan, B.; Luan, W.; Tu, S.-T. One-step synthesis of cubic FeS₂ and flower-like FeSe₂ particles by a solvothermal reduction process. *Dalton Trans.* **2012**, *41*, 772–776. [[CrossRef](#)]
39. Xu, J.; Xue, H.; Yang, X.; Wei, H.; Li, W.; Li, Z.; Zhang, W.; Lee, C.-S. Synthesis of Honeycomb-like Mesoporous Pyrite FeS₂ Microspheres as Efficient Counter Electrode in Quantum Dots Sensitized Solar Cells. *Small* **2014**, *10*, 4754–4759. [[CrossRef](#)]
40. Chakraborty, B.; Show, B.; Jana, S.; Mitra, B.C.; Maji, S.K.; Adhikary, B.; Mukherjee, N.; Mondal, A. Cathodic and anodic deposition of FeS₂ thin films and their application in electrochemical reduction and amperometric sensing of H₂O₂. *Electrochim. Acta* **2013**, *94*, 7–15. [[CrossRef](#)]
41. Khabbaz, M.; Entezari, M.H. Degradation of Diclofenac by sonosynthesis of pyrite nanoparticles. *J. Environ. Manag.* **2017**, *187*, 416–423. [[CrossRef](#)] [[PubMed](#)]

42. Xian, H.Y.; Zhu, J.X.; Liang, X.L.; He, H.P. Morphology controllable syntheses of micro- and nano-iron pyrite mono- and poly-crystals: A review. *RSC Adv.* **2016**, *6*, 31988–31999. [[CrossRef](#)]
43. Wang, Q.; Morse, J.W. Laboratory simulation of pyrite formation in anoxic sediments. *ACS Symp. Ser.* **1995**, *612*, 206–223. [[CrossRef](#)]
44. Li, Q.; Wei, Q.; Zuo, W.; Huang, L.; Luo, W.; An, Q.; Pelenovich, V.O.; Mai, L.; Zhang, Q. Greigite Fe₃S₄ as a new anode material for high-performance sodium-ion batteries. *Chem. Sci.* **2017**, *8*, 160–164. [[CrossRef](#)] [[PubMed](#)]
45. Blanchard, M.; Alfredsson, M.; Brodholt, J.; Wright, K.; Catlow, C.R.A. Arsenic incorporation into FeS₂ pyrite and its influence on dissolution: A DFT study. *Geochim. Cosmochim. Acta* **2007**, *71*, 624–630. [[CrossRef](#)]
46. Deditius, A.P.; Utsunomiya, S.; Renock, D.; Ewing, R.C.; Ramana, C.V.; Becker, U.; Kesler, S.E. A proposed new type of arsenian pyrite: Composition, nanostructure and geological significance. *Geochim. Cosmochim. Acta* **2008**, *72*, 2919–2933. [[CrossRef](#)]
47. Abraitis, P.K.; Patrick, R.A.D.; Vaughan, D.J. Variations in the compositional, textural and electrical properties of natural pyrite: A review. *Int. J. Miner. Process.* **2004**, *74*, 41–59. [[CrossRef](#)]
48. Xian, H.Y.; Zhu, J.X.; Tang, H.M.; Liang, X.L.; He, H.P.; Xi, Y.F. Aggregative growth of quasi-octahedral iron pyrite mesocrystals in a polyol solution through oriented attachment. *Crystengcomm* **2016**, *18*, 8823–8828. [[CrossRef](#)]
49. Liang, Y.X.; Bai, P.P.; Zhou, J.; Wang, T.Q.; Luo, B.W.; Zheng, S.Q. An efficient precursor to synthesize various FeS₂ nanostructures via a simple hydrothermal synthesis method. *Crystengcomm* **2016**, *18*, 6262–6271. [[CrossRef](#)]



© 2019 by the authors. Licensee MDPI, Basel, Switzerland. This article is an open access article distributed under the terms and conditions of the Creative Commons Attribution (CC BY) license (<http://creativecommons.org/licenses/by/4.0/>).